Implementation, Modelling and Verification of High-speed Mach-Zehnder Phase Modulators in an Open Access InP Foundry Platform

Y Durvasa Gupta, Guillaume Binet, Wouter Diels, Oliver Abdeen, Tom Gaertner, Moritz Baier and Martin Schell

Abstract—We present the introduction of high-speed phase modulators based on the quantum-confined Stark effect to the generic InP foundry platform at Fraunhofer HHI. An overview of the technological integration of the high-speed phase Mach-Zehnder modulators (MZM) to the existing generic foundry process is described. In addition, an electro-optical behavioral model for the high speed MZM, which gives insight into the influence of design parameters on performance, is discussed. The presented MZM structure with a traveling wave electrode length of 5 mm has a V_π of 1.4 V and a small signal electro-optic 3 dB bandwidth of 32 GHz. Large signal RF operation up to 80 Gbps is demonstrated. To the best of our knowledge, these are the highest-performance MZMs in an InP open access integrated photonics foundry platform.

Index Terms—modulators, electro-optic modulation, coherent transceiver, Indium Phosphide, semi-insulating substrate, integrated photonics.

Fig. 1: Schematic showing the epitaxial layers of the generic foundry process.

I. Introduction

WITH the increase in demand for streaming services and cloud storage platforms, large-capacity optical fibers are becoming ever more important in short- and middle-reach links, such as those in datacenter networks [1]. Coherent optical transceivers with fast modulators are key in fulfilling this demand and realizing them on an open access integrated platform provides a cost-effective solution. HHI not only has long standing expertise in developing high-speed phase Mach-Zehnder modulators (MZM) [2] but also offers its generic InP foundry process in the form of open access Multi-Project Wafer (MPW) runs via the JePPIX platform [3], [4]. This allows external customers to realize their optical interconnect application specific photonic integrated circuits (PICs) at a low cost and fast turn-around time. The generic foundry already offers DFB lasers with output power of 10 dBm, polarization rotators with polarization extinction ratio more than 16 dB over the entire C-band [5] and high speed photodetectors (PD) with small signal 3 dB bandwidth of 40 GHz [4].

High-speed MZMs have been reported in an integrated InP platform previously, on an open-access platform with an n-doped substrate [6] and in a generic foundry with a semi-
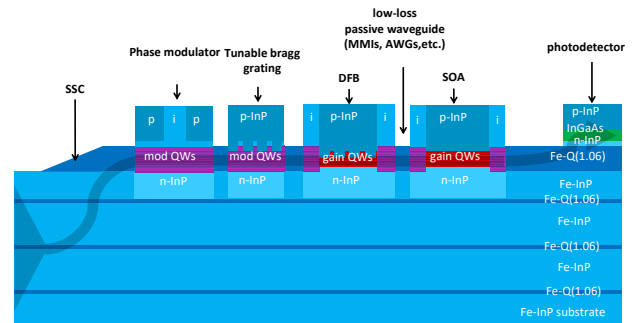
Y. D. Gupta, W. Diels, G. Binet, O. Abdeen and T. Gaertner are with Fraunhofer Heinrich Hertz Institute, Einsteinufer 37, 10587 Berlin, Germany. (e-mail for correspondence: ydurvasa.gupta@hhi.fraunhofer.de).

M. Schell is with the Fraunhofer Heinrich Hertz Institute, Berlin 10587, Germany, and also with the Technical University Berlin, Berlin 10623, Germany (e-mail: martin.schell@hhi.fraunhofer.de).

M. Baier, was with Fraunhofer Heinrich Hertz Institute, Einsteinufer 37, 10587 Berlin, Germany. He is now with KEEQuant GmbH, Gebhardtstr. 28, 90762 Fürth, Germany.

insulating substrate and multi quantum wells (MQWs) [7]. These modulators consist of both traces of a coplanar stripline (CPS) electrode contacting the modulator waveguides over the entire length. While straightforward, there is not much parameter space flexibility in device design, potentially resulting in a compromise between modulator performance and fabrication capabilities. Nevertheless, the modulators in [7] achieve high half-wave voltage-times-length (V_πL) and 3 dB bandwidth-times-length (f_{3dB}L) of 7 V-mm and 134 GHz-mm respectively.

This work presents the inclusion of traveling wave electrode (TWE) based MZMs to the HHI generic foundry. To this end, a dedicated multi quantum well (MQW) based modulator stack was integrated (Fig. 2). In this case, however, the TWEs consist of CPS electrodes periodically contacting the waveguides. Taking advantage of the increased parameter space, a better compromise between performance and fabrication capabilities is achievable resulting in a similar V_πL compared to [7] but a higher f_{3dB}L of 160 GHz-mm.

This paper presents the advances in our generic foundry platform and is organized in the following way: Section 2 describes the modification of the existing integration technology and the design of the high-speed MZM, Sections 3, 4 present simulation models developed to predict and improve the device performance, Section 5 discusses the MZM performance, and finally, Section 6 concludes the paper.

II. OVERHAULING THE HHI InP FOUNDRY PROCESS

Until 2020, the HHI generic foundry process consisted of an active layer stack (optical amplification, electro absorption) and a passive layer stack (low loss propagation) on a semi-insulating substrate. For the integration of the modulators, an additional 20 period InGaAsP/InP MQW layer stack optimized for phase modulation is introduced to the process flow. For low optical transmission loss, the absorption edge is set away from the operation wavelength. Furthermore, in order to achieve additive contributions of the electro-optic effects (Pockels effect and quantum-confined Stark effect) for TE input, the crystal orientation is changed from the existing [110] to [1$\bar{1}$0].
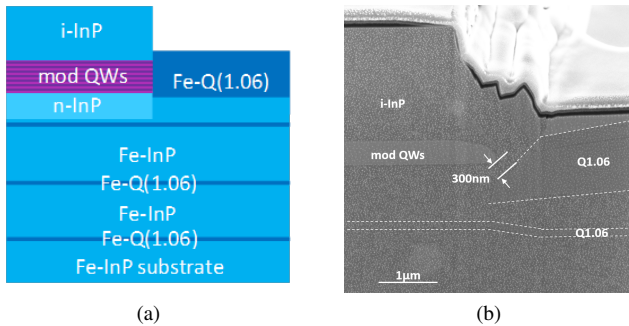

Fig. 2: a)Schematic representation. b) FIB-SEM photograph of the interface between the phase modulator MQW regrown with i-InP and the passive waveguide layers.

The integration process relies on a combination of butt-joint (BJ) regrowth steps where each grown material has different optical properties and serves the optimization of a specific building block [4]. The BJs connect the different waveguide architectures efficiently and with low reflections. Fig. 2 shows a cross-sectional illustration and Focused Ion Beam Scanning Electron Microscope (FIB SEM) picture of the BJ interface between the phase modulator MQW regrown with i-InP and the passive waveguide layers. These are followed in the process by a series of dry and wet chemical etching steps to define the active mesa structures, the different types of waveguides, the polarization elements, and the spot size converter. The process finishes with the passivation and metallization steps to contact the diodes, the heating elements, and to define the electrical routing.

Initially, the diluted waveguide, the n-doped buffer and the active layers are grown during the first epitaxial step on a semi-insulating substrate. The diluted waveguide consists of an unstrained super-lattice of Q1.06 InGaAsP and InP material. The active layers consist of a stack of 8 InGaAsP strained-compensated MQWs centered around 1540nm. These are designated gain-QW in Fig. 1. The wafer is then patterned by inductively coupled plasma (ICP) etching before growing the phase modulator MQW layers (mod-QW in Fig. 1 and Fig. 2). The BJ loss between the gain and phase modulator MQW is about 0.2 dB.

In the next step, the DFB and DBR gratings are defined by e-beam lithography and later etched in the semiconductor material by means of reactive ion etching (RIE). The DFB gratings are etched 90 nm in the gain MQW stack in order to define first-order complex coupled gratings over the C-band. This results in a DFB coupling coefficient κ of 550 cm^{-1}. The DBR gratings are etched 60 nm into the phase modulator MQW and result in a κ of 100 cm^{-1}. The p-doped cladding is regrown after that. The wafer is then patterned with a SiN mask and the p-doped cladding is etched selectively, followed by a regrowth of intrinsically doped InP (i-InP). This layer is used to define the TWE and enables low loss transmission in the phase modulator where the p-i-n diode is not needed [8]. Then, the wafer is patterned and etched once again. The following BJ regrowth contains the waveguide and the PD layers. The PD is based on evanescent coupling of light from the Q1.06 passive waveguide to the InGaAs absorbing layer above. The BJ loss between the phase modulator MQW and the passive waveguide is 1.5 dB. All layers are grown using Metal Organic Vapor Phase Epitaxy (MOVPE) in a production scale Aixtron AIX 2800-G4 reactor.
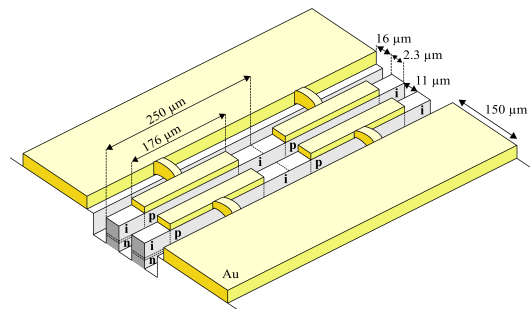

Fig. 3: Illustration of TWE EOPM sections.

After epitaxial growth, the receiver area is selectively etched and the mesa-structures are defined by lithography using both wet and dry etching. Three different passive waveguides are implemented with different index contrasts. The waveguides are all defined in SiN in a single step to ensure perfect alignment and are ICP-etched selectively. The different etch depth and mode confinement are described in [4]. As a final step, passivation of the active waveguides is performed to ensure high electrical isolation which is followed by four steps of metallization optimized to reduce parasitic capacitance and series resistance.

III. TRAVELING WAVE MACH-ZEHNDER MODULATOR

With the new modulator waveguide and transitions in place, a multitude of new building blocks could be introduced into the HHI generic foundry platform, with the TWE EO phase modulator (EOPM) as the most important (adapted from [9]). On the one hand it consists of two optical waveguides, in which intrinsic modulator sections are periodically alternated with p-doped sections. On the other hand, wide gold traces run next to the optical waveguides, periodically contacting the p-doped sections through air bridges, as shown in Fig. 3. A FIB SEM photograph of the top view of these electrodes is shown in Fig. 4. The number of sections, and as such the TWE length, can be chosen by the designer. At the ends of the line, the wide gold traces make 90 degree bends away from (and over) the optical waveguides.
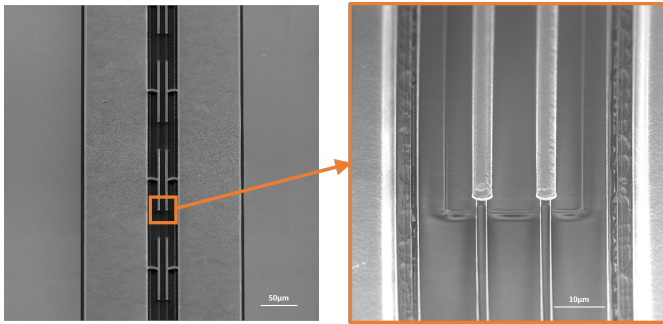
Fig. 4: Top view SEM picture of the TWE section. left: The outer transmission lines run parallel to the optical waveguides periodically contacting only the p-doped sections through air bridges. right: Close up view of metal contacting the p-doped waveguide section.

Fig. 5: Building blocks forming an MZM and DC electrical connections in the HHI generic foundry platform.

An RF-voltage over the line is, in principle, equally divided over the two waveguides diodes, which means both arms modulate equally but in antiphase, i.e. push-pull modulation. For high-frequency performance, the propagation constant γ_e and characteristic impedance Z_0 of the transmission line are engineered to match the propagation constant of the optical waveguide γ_o and the output impedance of the driver electronics respectively. For the latter, the industry standard of 50 Ω was chosen. A single-ended drive scheme is employed as it only requires a single 50 Ω termination whereas a differential-drive scheme with 2x25 Ω terminations would not be compatible to standard 50 Ω equipment. Both Z_0 and γ_e are heavily influenced by the capacitance-per-length of the line and therefore the fill factor of the p-doped sections, which in turn also determine the half-wave voltage (V_π) of the modulator. Note that because of the push-pull implementation, in which the capacitances of the diodes are connected in series, a larger fill factor is allowed compared to a single-drive implementation, in which the line voltage is applied over a single waveguide diode.

The TWE EOPM block requires an n-contact to provide access to the n-doped region of the stack in order to bias the waveguides. The electrical operating point should be chosen such that the diodes are always operated in reverse bias for the given AC-voltage swing. Moreover, increasing this operating point voltage increases the modulation strength (i.e. the change of refractive index per change of voltage), but also the optical losses. Adding additional multi-mode interference (MMI) couplers to the input and output optical ports forms a high-speed MZM. Electro-optical DC phase shifters, which are p-doped modulator waveguides, should also be included to set the working point of the modulator. Finally, an integrated 50 Ω resistor (EOPMTermination) can optionally terminate the electrical output port on-chip. An illustration of the building blocks forming the MZM and the DC electrical equivalent is shown in Fig. 5.

IV. ELECTRO-OPTICAL MODEL

With the process in place, it is important to optimize the layout for high performance. To this end, accurate modelling
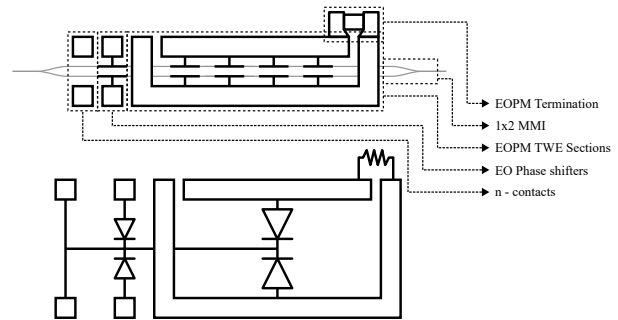
of the traveling wave phase modulator is imperative. For the traveling wave electrode modulator, the effective group index vs voltage characteristics of the waveguide $\tilde{n}_{eff}(V)$ together with the voltage distribution over the optical waveguides $\tilde{V}(z, f)$ are essential parameters to calculate the EO frequency response. The former is largely dominated by the complex refractive index of the MQW stack ($\tilde{n}_{MQW}(V)$), which in turn can be simulated with a k.p simulator such as Lumerical MQW or Nextnano. Alternatively, this refractive index can be extracted experimentally by incorporating the waveguides in an interferometer, which inherently is the case in a Mach-Zehnder modulator. Calculating the voltage distribution requires diode-specific information such as the capacitance-per-length, C/l, and the resistances-times-length, Rl, of the p- and n-sides. Similar to the refractive index, these values can either be calculated in a semiconductor solver or determined experimentally.

Once these values have been determined, the modulator can be completely simulated electrically in finite element method simulators, such as Ansys HFSS. Following section talks about the simulations for 5 mm long MZM. The waveguide diode parameters are incorporated through lumped RLC and impedance boundary conditions on sheets. This simulation model readily produces scattering parameters, which can easily be verified with electrical measurement results taken with a vector network analyzer (VNA). At the same time, the model can also yield $\tilde{V}(z, f)$ by integrating the electric fields over the waveguide lines. For instance, Fig. 6 shows the calculated voltage distribution for 1 GHz and 30 GHz.

A. Basic circuit equivalent model

While the HFSS model is very accurate, it is not very flexible (e.g. when changing the MZM dimensions) and is time- and computationally intensive. For this reason, a circuit model is proposed, based on transmission lines, as seen in Fig. 7 (a).

A distinction is made between the outer transmission lines (OTLs) and the inner transmission lines (ITLs). The OTLs consist of the large gold traces connecting the input and output ports of the modulator, whereas the ITLs consist of the narrow gold traces on top of the waveguides. The ITLs are periodically connected to the OTLs via air bridges, which
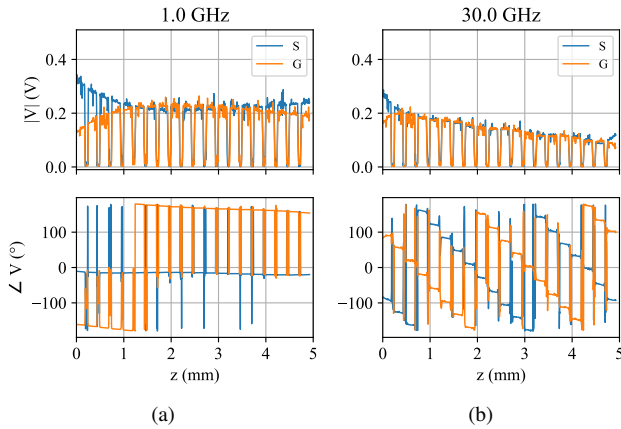
Fig. 6: Extracted voltage distribution from HFSS model. (a) 1 GHz (b) 30 GHz
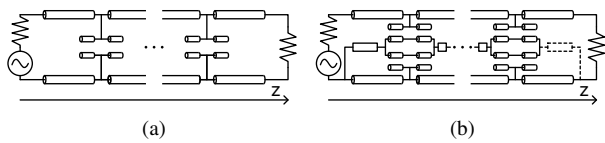

Fig. 8: Calculated voltage distribution from extended circuit model. (a) 1 GHz (b) 30 GHz

Fig. 7: (a) Circuit model of TWE modulator. (b) Modified circuit model to include n-contact biasing.

Fig. 9: Simulated EE response of MZMs with different TWE lengths.

in this model are assumed to be shorts. For given geometric dimensions and diode parameters, a mode solver should run only once to calculate the characteristic impedance Z_0 and propagation constant γ of these lines. Once these are found, the voltage distribution on the lines can be calculated using only Kirchhoff's equations. Furthermore, the amount of phase modulator sections can readily be parameterized using scripted netlist generation.

B. Extended circuit equivalent model

The basic model in Fig. 7 (a) assumes that the voltage over the two waveguides is identical and in antiphase i.e. perfect push-pull. However, as could already be seen in the HFSS results in Fig. 6, this is not entirely the case, especially near the ends of the line. This behavior can be explained by the biasing of the n-contact. This connection introduces another path for the currents to flow to the ground node, especially at low frequencies. While these effects are already included in the HFSS model, the circuit model (Fig. 7 (b)) requires some adjustments. By considering the ITLs as a series connection of a pair of transmission lines with half the original characteristic impedance, the n-doped regions of the ITLs become accessible circuit nodes. Fig. 8 shows the calculated voltage distribution when there is a 250 Ω impedance between the n-contact and the ground node, and 100 Ω impedance between the n-regions of adjacent modulator sections, which shows good agreement with the HFSS model. While true push-pull operation can be approached by adding an additional impedance between the n-contact and the ground node, there is always some deviation near the n-contact itself.
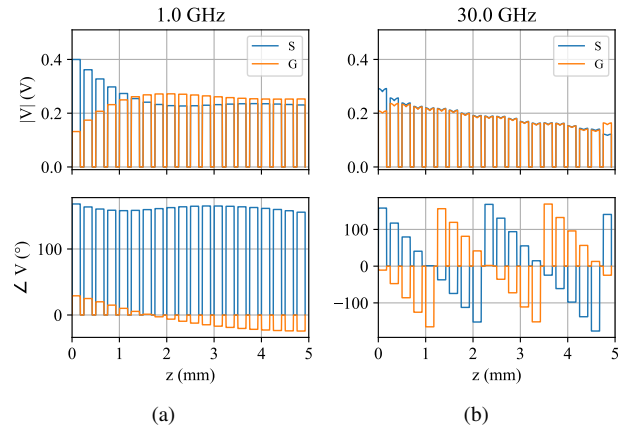
$$V_r(z, f, \theta) = V_{DC} + |\tilde{V}(z,f)|cos(\angle \tilde{V}(z,f) + \theta)$$
$$E_{out}(f, \theta) = E_{in}e^{-j\frac{2\pi}{\lambda_0}\int_0^L \tilde{n}_{eff}(V_r(z,f,\theta+2\pi f\frac{z}{v_o}))dz} \quad (1)$$

Reflection (S11) and electro-electrical insertion loss (S21) magnitudes calculated with the extended equivalent circuit model for various TWE lengths are shown in Fig. 9. As can be seen, the reflection becomes independent of the line length and depends only on the characteristic impedance at high frequencies due to the electrical propagation losses. With the voltage distributions and optical waveguide group indices determined, the optical phasor of the electrical field at the output of the modulator arms E_{out} can be calculated. Note that as $\tilde{V}(z,f)$ is already an (electrical) phasor, a real voltage distribution $V_r(z, f, \theta)$ must be defined to differentiate between the electrical and optical oscillation frequency. E_{out} can then be calculated by integrating over the line, whilst taking into account that the optical wave travels at a velocity v_o, as written in (1) [10]. In this formula, E_{in} is the optical phasor at the input of the modulator arm and L is the length of the modulator. In this equation, E_{in} is the optical phasor at the input of the modulator arm and L is the length of the modulator.
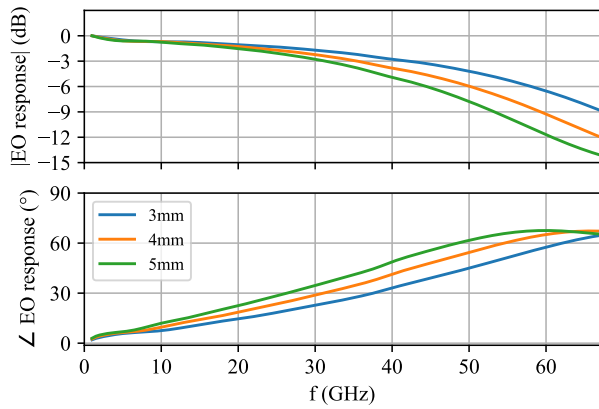
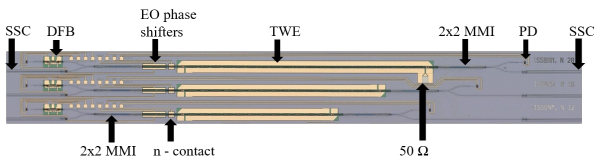Fig. 10: Simulated EO response of MZMs with different lengths.

Fig. 11: Photograph of MZMs with TWE lengths of 3 mm, 4 mm and 5 mm.

The optical output phasors are calculated over an entire θ cycle from 0 to 2π. From the resulting dataset, harmonics can be derived, yielding the electro-optic frequency response of the parameter of interest. For example, Fig. 10 shows the EO frequency response of the MZM output intensity for various lengths. With the extended circuit equivalent model in place, the performance of the MZM can be simulated. This is helpful in optimizing the electrical design and improving the device performance. Also, including the transfer function of the MZM RF response in the PDK enables PIC designers to simulate the transient response of the device for arbitrary waveforms.

V. RESULTS AND DISCUSSION

The initial results have already been published in [11] and since then the process has been optimized and this section presents the results for the latest devices.

A. DC characterization

Fig. 11 shows optical microscope image of the devices used for characterization. MZMs with different TWE lengths are on the test cell. Each test structure is a PIC consisting of several passive (spot-size converter (SSC), 2x2 MMI, waveguide, PD), active (DFB laser, MZM, EO phase section) and electrical (50 Ω termination) building blocks that are offered on the HHI generic foundry platform. The DFB, centered at 1550 nm, on one arm of the MZM serves as optical input and the other arm of the MZM is equipped with SSC for coupling light using a single mode butt fiber.

A completely electrical DC characterization is presented here and uses the integrated DFB and PD. The DFB emits
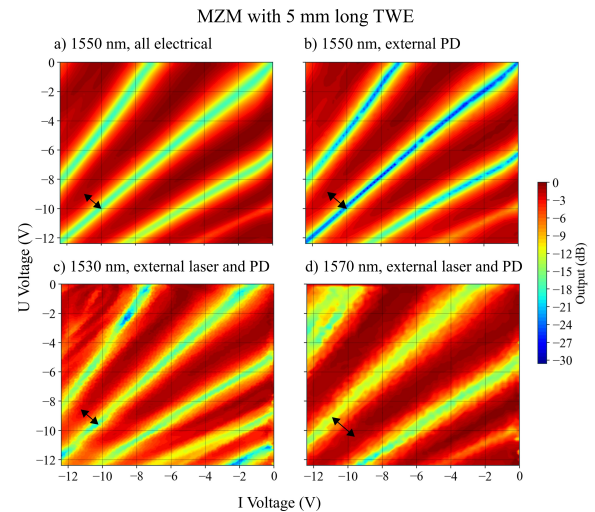

Fig. 12: DC extinction ratio maps for different wavelengths.

TE polarized light as it has strained quantum wells [4]. The output optical power from one of the arms of the MZM is recorded using the integrated PD. Reverse bias voltages are applied between the two TWE ports (U, V) independently with the n-contact pad connected as ground. The EO phase shifters were used to shift the pattern into the minimum transmission point (SW-NE diagonal on the valley). The resulting extinction ratio (ER) map for the MZM with a 5 mm long TWE section is shown in Fig. 12a. The V_π of the ER map is read parallel to the NW-SE diagonal when the structure is driven in push-pull operation. V_π can be deduced from the plot to be 1.4 V at a bias of -10 V (as indicated by the black line in Fig. 12a), which translates to a $V_\pi L$ of 0.7 V-cm. Using an external laser source at 1550 nm (TE-polarized) and biasing one of the TWE arms for maximum optical transmission, the insertion loss for the 5 mm long MZM is measured to be 12.5 dB. The fiber coupling loss to the SSCs is 4 dB (with reference to fiber-fiber transmission), the propagation loss of the phase modulator MQW section is 4 dB, and each arm has two BJ transitions from passive waveguide to the phase modulator MQW with a combined loss of 3 dB. Passive components (waveguide, couplers, bends) contribute a loss of ~1.5 dB.

While characterizing the MZM with the integrated PD, the ER is limited by the light propagating in the substrate mode. From Fig. 12a, the maximum ER for the 5 mm long MZM is 20 dB. However, light coupled into a single mode fiber eliminates the substrate mode extensively and as can be seen from Fig. 12b, a higher ER up to 31 dB is measured using an external PD. For demonstrating the DC performance over the C-band, the extinction ratio maps for the optical signal at 1530 nm (Fig. 12c) and 1570 nm (Fig. 12d) have been measured using an external laser source (TE-polarized) and an external PD. The half-wave voltages for 1530 nm and 1570 nm input are 1.2 V and 1.7 V respectively.

All-electrical characterization is possible only due to the integrated laser and detector. It is highly beneficial in saving time and cost for automating the selection of good dies on a wafer level for large-scale production. High-speed PDs were not included in the PIC used in this work and were introduced
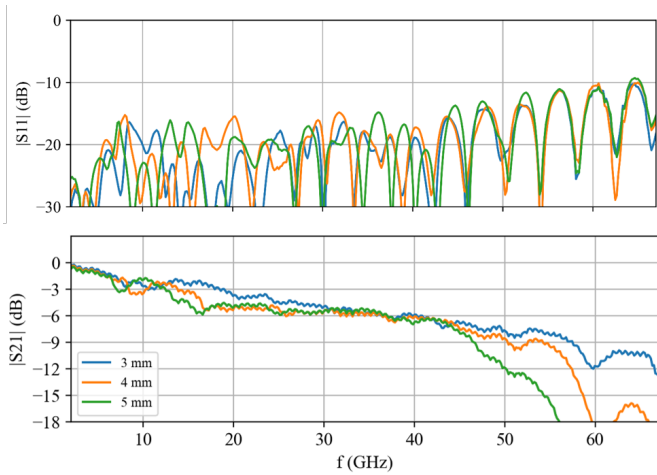
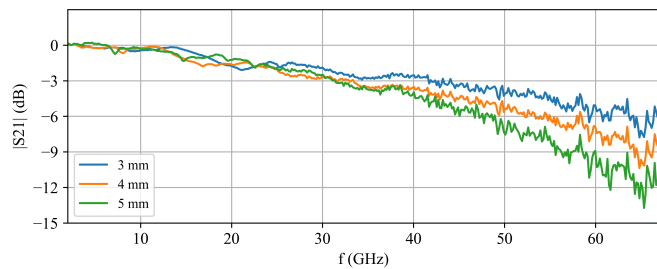Fig. 13: Measured small signal EE response of MZMs of different lengths.

Fig. 14: Measured small signal EO response of MZMs of different lengths.

Fig. 15: Optical eye diagrams for 5 mm long MZM.

only in later designs. Therefore, the RF characterization presented in the following sections is not all-electrical but the HHI generic foundry is equipped with PDs that support speeds upto 40 GHz enabling all-electrical RF characterization as well.

B. RF characterization

The electro-electrical (EE) S-parameters for the MZMs of different lengths are measured with a VNA and the results are plotted in Fig. 13. The RF-probes, which were used to contact the TWE electrical ports, are digitally de-embedded for these plots. The small signal electro-optic (EO) 3 dB bandwidth is measured using the VNA connected to a light component analyzer (LCA) module. An electrical GS probe is used for applying the high speed signal to one electrode end of the modulator. The other electrode end for the 5 mm long MZM is terminated with an on-chip 50 Ω resistor. A 50 Ω terminated probe is used for the other two MZMs. An optical amplifier and a passive optical bandpass filter have been used for all RF characterization. A constant voltage source is used for biasing the MZM to the working point of 8 V. The measured small signal RF response of the MZMs for an input light of 1550 nm are plotted in Fig. 14. The electrical reflections are below -10 dB at least until 60 GHz. The electro-optic 3 dB bandwidths for the 3 mm, 4 mm and 5 mm long MZMs are 42 GHz, 34 GHz and 32 GHz respectively.
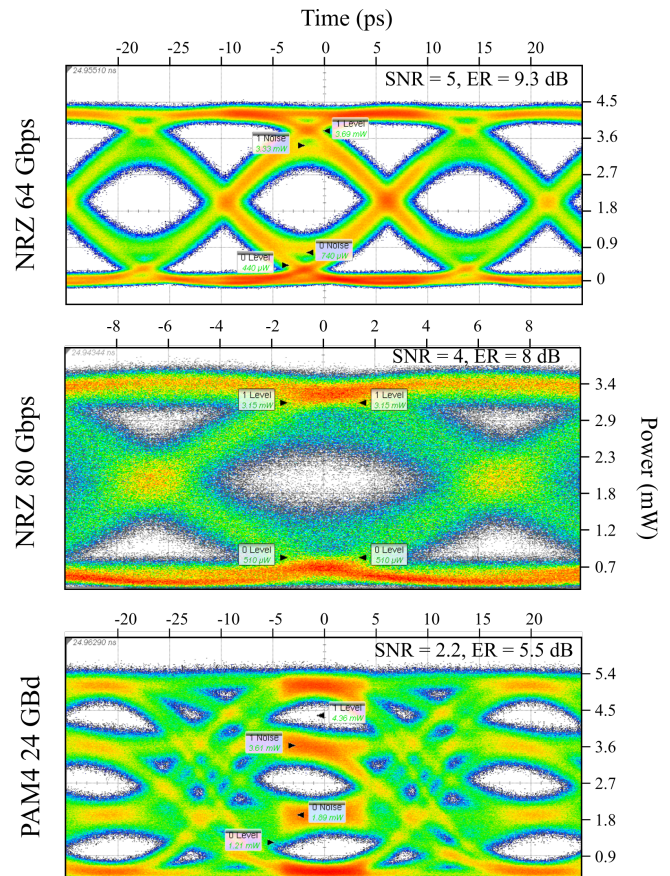
The slope of the EO response is slightly lower than that of the EE response as the latter corresponds to the voltage at the end of the line whereas the former encapsulates the integration of the voltage over the entire line.

C. Large signal characterization

In [11], the 5 mm long device did not support 80 Gbps NRZ operation. With the improved devices in this work, the 5 mm long MZM is characterized. The SSC arms of the MZM are used for accessing it optically. A bit pattern generator (limited to a bit rate of 65 Gbps) is used to generate NRZ sequences and the output voltage (0.5 V) is boosted to 1.4 V$_{pp}$ using a 66 GHz amplifier. These measurements do not involve any digital pre-distortion or post processing. The MZM is biased at the working point of 10 V and Fig. 15 shows the measured optical eye diagrams for a bit rate of 64 Gbps. The SNR as evaluated by the optical oscilloscope is 5 and the ER is 9.3 dB. For higher bit rates, a MUX is included in the electrical circuit. Fig. 15 shows the optical eye for 80 Gbps NRZ operation with an SNR of 4 and ER of 8 dB. The drop in SNR for the 80 Gbps case can be attributed to the MUX. 24 GBd PAM4 modulation has also been tested with the device (Fig. 15) by including a 3-bit 32 GBd DAC. Beyond 24 GBd PAM4, the optical eye was noisy and we are currently investigating the source of the noise which we believe to be from the measurement apparatus.

D. MZM performance

The 3 dB bandwidth and V_π are crucial parameters to gauge the performance of the phase modulator and both are dependent on the modulator length. The length of the modulator cannot be increased arbitrarily in order to decrease the V_π without significantly degrading the 3 dB bandwidth. The periodically loaded TWE based design becomes crucial in this case, as the phase mismatch between the optical wave and electrical wave is eliminated at regular intervals, hence, making longer modulator lengths a viable option. The figure of merit (FOM), 3 dB bandwidth/V_π, eliminates the length dependence of the individual parameters. We published the initial results previously [11], where the FOM was 15 GHz/V and now for the 5 mm long MZM, this figure is 23 GHz/V. We expected the increase in performance due to optimization in the metallization process. The FOM for the device presented is >6 times compared to [6] (3.4 GHz/V) and better than [7] (19 GHz/V).

VI. Conclusion

The highest performance modulators (23 GHz/V) that are now available in the open access InP HHI generic foundry platform have been presented. NRZ operation up to 80 Gbps has been demonstrated for a 5 mm long MZM. The MZM has a small signal electro-optic RF 3 dB bandwidth of 32 GHz, a V_π of 1.4 V, and an insertion loss of 12.5 dB (including butt-joint transitions and fiber coupling). The DC performance of the device has improved by 50% compared to the devices we previously reported [11] and is at par with that of the state of the art phase modulators at HHI [2]. Further optimization of the metallization process should result in decrease in electrical losses and improved RF performance. With modifications to the measurement apparatus and electrical handling of the device, there is a lot of scope for improvement in the large signal performance as well. We believe that the insertion loss can be significantly lowered with improvements in waveguide lithography and the modulator-passive butt joint transition. The high-speed modulators that are now conceivable on the HHI generic foundry platform can help achieve low-cost, complex multi-level coherent transmission systems on an InP photonics integrated circuit.

Acknowledgment

References

[1] T. Cisco *et al.*, "Cisco annual internet report," 2020.

[2] S. Lange, S. Wolf, J. Lutz, L. Altenhain, R. Schmid, R. Kaiser, M. Schell, C. Koos, and S. Randel, "100 gbd intensity modulation and direct detection with an inp-based monolithic dfb laser mach–zehnder modulator," *J. Lightwave Technol.*, vol. 36, no. 1, pp. 97–102, Jan 2018. [Online]. Available: https://opg.optica.org/jlt/abstract.cfm?URI=jlt-36-1-97

[3] "JePPIX: Joint European Platform for Photonic Integration of Components and Circuits. ," www.jeppix.eu.

[4] F. M. Soares *et al.*, "Inp-based foundry pics for optical interconnects," *Applied Sciences*, vol. 9, no. 8, 2019.

[5] M. Baier, F. M. Soares, T. Gärtner, M. Moehrle, and M. Schell, "Fabrication tolerant integrated polarization rotator design using the jones calculus," *J. Lightwave Technol.*, vol. 37, no. 13, pp. 3106–3112, Jul 2019. [Online]. Available: https://opg.optica.org/jlt/abstract.cfm?URI=jlt-37-13-3106

[6] A. Meighan, M. J. Wale, and K. Williams, "High-density coplanar strip-line mach-zehnder modulators in a inp generic platform," in *2021 European Conference on Optical Communication (ECOC)*, 2021, pp. 1–3.

[7] A. Meighan, L. Augustin, M. J. Wale, and K. A. Williams, "High-density 100 ghz-class mach-zehnder modulators integrated in a inp generic foundry platform," in *Conference on Lasers and Electro-Optics*. Optica Publishing Group, 2022, p. SF4M.6. [Online]. Available: https://opg.optica.org/abstract.cfm?URI=CLEO_SI-2022-SF4M.6

[8] H. C. Casey and P. L. Carter, "Variation of intervalence band absorption with hole concentration in p-type inp," *Applied Physics Letters*, vol. 44, no. 1, pp. 82–83, 1984. [Online]. Available: https://doi.org/10.1063/1.94561

[9] H. Klein, H. Chen, D. Hoffmann, S. Staroske, A. Steffan, and K.-O. Velthaus, "1.55m mach-zehnder modulators on inp for optical 40/80 gbit/s transmission networks," in *2006 International Conference on Indium Phosphide and Related Materials Conference Proceedings*, 2006, pp. 171–173.

[10] G. Ghione, *Semiconductor Devices for High-Speed Optoelectronics*. Cambridge University Press, 2009.

[11] Y. D. Gupta, G. Binet, W. Diels, J. A. Heibach, J. Hogan, M. Baier, and M. Schell, "Highest performance phase modulators on an open access inp platform," in *European Conference on Optical Communication (ECOC)*, 2022, p. TU4E.6.